Spatial Orientations of Hydraulically Conductive Shear Natural Fractures for an Arbitrary Stress State: an Analytical Study

N. V. Dubinya[1,2]

[1] Moscow Institute of Physics and Technology, Russia, Dolgoprudny, Institutskiy per., 9, 141701.

[2] Schmidt Institute of Physics of the Earth of the Russian Academy of Sciences, Russia, Moscow, B. Gruzinskaya str., 10-1, 123242.

Corresponding author: Nikita Dubinya (Dubinya.NV@gmail.com)

Key Points:

- Hydraulic conductivity of natural fractures is related to current stress state
- Orientations of conductive fractures are obtained for an arbitrary stress tensor
- Various stress regimes are related to different patterns of conductive fractures.

Abstract

The paper focuses on spatial orientations of hydraulically conductive shear fractures existing in naturally fractured fluid saturated rocks. Hydraulic conductivity of such fractures is considered from the current stress state of these rocks. The concept of critically stressed fractures is generally used to establish such relationship. The paper presents an analytical solution to the problem of obtaining all possible spatial orientations of critically stressed fractures for an arbitrary stress tensor. The proposed solution is explicit, providing an opportunity to predict the spatial orientations of hydraulically conductive fractures based on results of any sort of solutions to geomechanical problems considering naturally fractured rocks. The obtained results may be directly used for planning the development of oil fields, characterized by considerable contribution of fractures to permeability in cases when geomechanical modeling takes place. Several examples of applying the obtained solution in practice are presented in the paper: critically stressed fractures spatial orientations are considered for cases of gradual changes in stress tensor components under specific conditions providing an understanding of the main tendencies in these spatial orientations.

Plain Language Summary

Nowadays naturally fractured reservoirs are being developed in order to maintain and increase the level of oil production. Natural fractures tend to provide the best paths for oil to flow, yet it is a complicated problem to predict which fractures will provide such paths and which will not. It appears that many factors influence these fractures including so-called geomechanical factors – stresses and pressures acting at reservoir depth. While modern approaches make it possible to predict the stress state of reservoirs, but relationship between stresses and oil filtration paths remains a problem. The paper presents an analytical solution for spatial orientations of hydraulically conductive natural fractures in an arbitrary stress state. This solution can find its applications in a variety of areas in petroleum engineering including forecast of fractured zones in reservoir, estimation of stress state of the upper layers of the Earth's crust based on well logging data, hydrocarbon migration and others.

1 Introduction

The study is devoted to the problem of developing hydrocarbon reservoirs characterized by considerable contribution of natural fractures existing in fluid-saturated rock masses to their hydraulic properties. The main question of the paper is: how is it possible to use the existing approaches to reservoir behavior modeling in order to understand which reservoir zones are perspective for development due to existence of majority of natural hydraulically conductive fractures, and what are the preferable spatial orientations of these fractures? The latter point is extremely important for naturally fractured reservoir development as hydraulically conductive fractures provide filtration paths for fluid.

In the current study the stated question is answered from the point of view of geomechanical modeling. The approaches to three- and four-dimensional modeling of geomechanical processes taking place in the reservoirs (including fractured rocks) are now well-developed in the industry; there are algorithms for modeling the stress-strain state of a reservoir on different stages of development (Kolditz et al., 2016; Zhu et al., 2016).

There are a number of studies devoted to using the results of geomechanical modeling for analyzing the hydrodynamic properties of fractured rocks based on the concept of critically stressed fractures. This concept was proposed by Barton et al. (1995). According to the definition given in this paper, a fracture is considered to be critically stressed if shear stress acting on its surface is large enough for a slip to occur alongside the fracture's surface whenever differential stress is slightly increased. In order to determine whether a given fracture is critically stressed or not, one has to know the friction coefficient of the rock alongside with shear and normal stresses acting on its surface. These stresses, in turn, may be calculated if spatial orientation of the fracture and all components of the stress tensor in its vicinity are known. Barton et al. (1995) proved that critically stressed fractures are closely related to hydraulically conductive fractures by studying a well characterized by a high quality of well logs and existence of a reliable estimation of stress profiles. Classification of critically stressed and non-critically stressed fractures has been carried out revealing that the majority of critically stressed fractures tend to be hydraulically conductive as well. Hydraulic conductivity of particular fractures was estimated based on special well logs data. As a result, the following hypothesis was formulated: fractures which are critically stressed under current stress state tend to be hydraulically conductive and

non-critically stressed fractures tend to be non-hydraulically conductive. This hypothesis was later proved to be valid for different hydrocarbon reservoirs (Hickman et al., 1997; Townend & Zoback, 2000; Ito & Zoback, 2000; Rogers, 2003; Ligtenberg, 2005; Mattila & Follin, 2019) and geothermal fields (Davatzes & Hickman, 2010; Davidson et al., 2012; Massiot et al., 2017).

This hypothesis was used as a basis for an algorithm of optimizing the well production. One-dimensional geomechanical models are constructed on the basis of well logs data. These models include stress profiles along the well trajectory, which are subsequently used to predict zones containing critically stressed and, accordingly, hydraulically conductive fractures (Schwab et al., 2017; Bayuk et al., 2019; Chan et al., 2019). It should be mentioned that the results of detailed studies carried out in some regions (Fisher et al., 2003; Sathar et al., 2012; Bisdom et al., 2016) prove that the hypothesis of a relationship between critically stressed and hydraulically conductive fractures is not reliable in some cases. It is caused by geological factors, complex history of stress-strain state evolution in the region, and nonlinear rheological effects not taken into account in critically stressed fractures concept.

The concept of critically stressed fractures is also used for solving the inverse problem of stress estimation based on geophysical data for solving the important problems of wellbore stability (Ito et al., 2002; Dubinya & Ezhov, 2017; Dubinya, 2019). In this case the inverse problem is formulated as follows: one needs to reconstruct the stress profiles along the trajectory of a certain well based on the given information on which natural shear fractures in its vicinity are critically stressed, and which ones are not. The following algorithm is generally used in these studies mainly devoted to reconstruct stress profiles along the well trajectory. On the first step data obtained from special well logging techniques are used for determination of spatial orientations of all natural shear fractures observed in the well vicinity (Silva et al., 2003). Then estimations of some properties of well surrounding rock mass (temperature profiles (Ito et al., 2002), resistivity and acoustic properties distributions (Dubinya & Ezhov, 2017), or elastic moduli profiles (Dubinya, 2019)) are used to classify fractures as critically stressed or non-critically stressed. Finally, the profiles of principal stresses are adjusted in a way to obtain the best match between critically stressed fractures classification based on well logs, and the same classification based on stress profiles.

To sum up, critically stressed fractures concept is generally used in different areas of hydrocarbon reservoir geomechanics in cases of naturally fractured rock. The strong relationship between critically stressed and hydraulically conductive fractures increases the value of geomechanical modeling results as they give certain assumptions on fluid filtration.

The current paper presents a mathematical algorithm for direct calculation of all the possible spatial orientations of critically stressed fractures for an arbitrary given stress tensor. As far as an arbitrary stress tensor is considered, the hypothesis of one principal axis of stress tensor being subvertical, which is often used in problems of reservoir geomechanics (Zoback, 2007), may be avoided. It broadens the opportunities of critically stressed fractures analysis for solving the problems of fractured reservoirs development. The solution can find its applications in a variety of areas in petroleum engineering including forecast of fractured zones in reservoir, estimation of stress state of the upper layers of the Earth's crust based on well logging data, hydrocarbon migration and others.

2 Theory

According to initial definition given by Barton et al. (1995) a fracture is referred to as critically stressed, if normal and shear stresses acting on its surface satisfy the raw friction criterion:

$$\tau_n \geq \mu \cdot \sigma_n. \quad (1)$$

Here τ_n is shear stress acting on the fracture plane; σ_n is normal stress acting on the fracture plane; μ is friction coefficient of the rock mass. The value of friction coefficient μ is often defined as 0.6 following the well-known experiments (Byerlee, 1978) yet it is necessary to carry out special experiments to precisely estimate it for the specific rock. This coefficient is not specified for the analytical solution of the critically stressed fractures spatial orientations problem. In the most sections of this paper μ will be 0.6 as well.

Let's consider a volume of rock mass containing a number of microcracks. This c volume is characterized by an arbitrary stress tensor σ_{ij} with its principal components denoted as σ_1, σ_2, and σ_3. The following notation is used hereafter: compression is regarded as positive and $\sigma_1 \geq \sigma_2 \geq \sigma_3$. As fluid-saturated rock masses are studied in the paper, all the stresses will be considered as effective in terms of theory of poroelasticity (Biot, 1955; Coussy, 2004). All fractures and

129 microcracks will be considered as planes and their spatial orientations will be described using the
130 vectors normal to these planes or normal vectors.

131 In this paper critically stressed fractures will be often analyzed with the usage of Mohr's
132 diagram (Fig. 1) where axes represent the magnitudes of normal and shear stresses acting on any
133 plane. The given values of principal stresses σ_1, σ_2, and σ_3 make it possible to construct Mohr's
134 circle shown as a solid black line in Fig. 1. It can be shown that a dot representing any fracture
135 existing in the given stress state (with fixed principal stresses) is to stay inside the area bordered
136 by Mohr's circle.

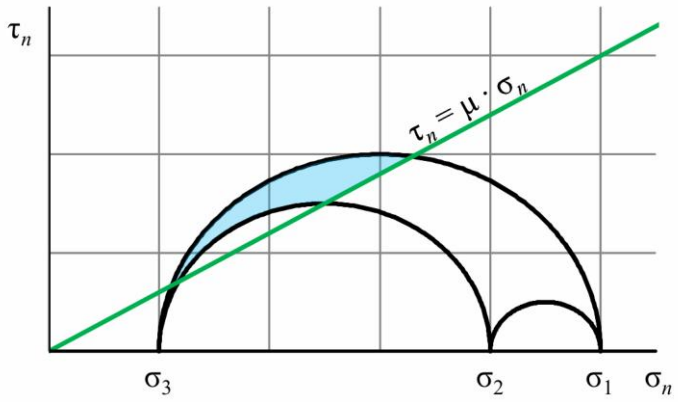

137

138 **Figure 1.** Schematic representation of critically stressed fractures at Mohr's diagram.

139 Raw friction law (1) is represented by solid green line in Fig. 1. Respectively, dots,
140 representing all the fractures with criterion (1) being satisfied, are to be above the green line. As
141 a result, dots representing critically stressed fractures are to stay inside a limited domain shown
142 in blue in Fig. 1.

143 In order to calculate normal and shear stresses acting on a plane with a given spatial
144 orientation one has to know the full stress tensor acting in the elementary volume containing this
145 plane. Normal and shear stresses may be calculated as:

146 $$\sigma_n = \sigma_2 + l^2(\sigma_1 - \sigma_2) + n^2(\sigma_3 - \sigma_2), \quad (2)$$

147 $$\tau_n^2 = \left(\frac{\sigma_2 - \sigma_3}{2}\right)^2 + l^2(\sigma_1 - \sigma_2)(\sigma_1 - \sigma_3) - \left(\sigma_n - \frac{\sigma_2 + \sigma_3}{2}\right)^2, \quad (3)$$

148 where l is the cosine of an angle between normal vector to a considered plane and
149 direction of maximum principal stress σ_1; n is the cosine of an angle between normal vector to a

considered plane and direction of minimum principal stress σ_1. l and n will be referred to as direction cosines of a normal vector to a fracture's plane or simply direction cosines hereafter. The pair of normal and shear stresses provide coordinates to the dot representing a fracture on Mohr's diagram. It should be noted, that normalized Mohr's diagram may be used for analysis as principal stresses are linearly included into equations (2) and (3).

The following problem may be solved. For the given principal stresses magnitudes σ_1, σ_2, and σ_3 one needs to find the variety of direction cosines l and n providing normal σ_n and shear τ_n stresses satisfying criterion (1). Equations (2) and (3) defining a dot on Mohr's diagram are equivalent to a system of two equations:

$$\tau_n^2 + \left(\sigma_n - \frac{\sigma_2+\sigma_3}{2}\right)^2 = \left(\frac{\sigma_2-\sigma_3}{2}\right)^2 + l^2(\sigma_1-\sigma_2)(\sigma_1-\sigma_3), \quad (4)$$

$$\tau_n^2 + \left(\sigma_n - \frac{\sigma_1+\sigma_2}{2}\right)^2 = \left(\frac{\sigma_1-\sigma_2}{2}\right)^2 + n^2(\sigma_3-\sigma_1)(\sigma_3-\sigma_2). \quad (5)$$

These equations have a geometrical meaning of the intersection point of two circles with centers having coordinates $(0; (\sigma_1 + \sigma_2)/2)$ and $(0; (\sigma_2 + \sigma_3)/2)$, and radii $(\sigma_1 - \sigma_2)^2/4 + n^2(\sigma_3 - \sigma_1)(\sigma_3 - \sigma_2)$ and $(\sigma_2 - \sigma_3)^2/4 + l^2(\sigma_1 - \sigma_2)(\sigma_1 - \sigma_3)$. Zero values of l and n are related to two small Mohr's circles themselves; gradual increase of these cosines provides an increase in circles' radii.

If a gradual increase of direction cosine n is considered, the first critically stressed fracture will emerge at the moment of the first intersection between circle (5) and the raw friction law line $\tau_n = \mu \cdot \sigma_n$. The corresponding value of direction cosine n is:

$$n_A = \sqrt{\frac{\tau_n^{A2} + \left(\sigma_n^A - \frac{\sigma_1+\sigma_2}{2}\right)^2 - \left(\frac{\sigma_1-\sigma_2}{2}\right)^2}{(\sigma_3-\sigma_1)(\sigma_3-\sigma_2)}}, \quad (6a)$$

$$\sigma_n^A = \frac{\sigma_1+\sigma_2}{2(\mu^2+1)}, \quad (6b)$$

$$\tau_n^A = \mu \cdot \sigma_n^A. \quad (6c)$$

The upper index A in these sequation represents the name of the point of intersection between circle (5) with radius (6a) and raw friction law.

It should be noted that technically this point may lie outside the area bordered by Mohr's circle preventing these stresses to be realized on the plane of any fracture. That means that the values of direction cosine *n* are also determined by intersections between the outer Mohr's circle and raw friction law. Let the outer Mohr's circle intersect the raw friction law at points *B* and *C* with point *C* staying to the right (Fig. 2a and 2b). Point A with coordinates calculated from equation (6) is given on these figures as well.

The values of normal and shear stress at points *B* and *C* and the corresponding value of direction cosine *n* are equal to:

For point *B*:

$$n_B = \sqrt{\frac{\tau_n^{B2} + \left(\sigma_n^B - \frac{\sigma_1+\sigma_2}{2}\right)^2 - \left(\frac{\sigma_1-\sigma_2}{2}\right)^2}{(\sigma_3-\sigma_1)(\sigma_3-\sigma_2)}}, \tag{7a}$$

$$\sigma_n^B = \frac{\sigma_1+\sigma_3 - \sqrt{(\sigma_1+\sigma_3)^2 - 4\sigma_1\sigma_3(\mu^2+1)}}{2(\mu^2+1)}, \tag{7b}$$

$$\tau_n^B = \mu \cdot \sigma_n^B. \tag{7c}$$

For point C:

$$n_C = \sqrt{\frac{\tau_n^{C2} + \left(\sigma_n^C - \frac{\sigma_1+\sigma_2}{2}\right)^2 - \left(\frac{\sigma_1-\sigma_2}{2}\right)^2}{(\sigma_3-\sigma_1)(\sigma_3-\sigma_2)}}, \tag{8a}$$

$$\sigma_n^C = \frac{\sigma_1+\sigma_3 + \sqrt{(\sigma_1+\sigma_3)^2 - 4\sigma_1\sigma_3(\mu^2+1)}}{2(\mu^2+1)}, \tag{8b}$$

$$\tau_n^C = \mu \cdot \sigma_n^C. \tag{8c}$$

That means that the values of direction cosine *n* for critically stressed fractures are to stay inside the following limits:

$$n \in \left[\max(n_A; n_C); \quad n_B\right], \tag{9}$$

where the values of n_A, n_B, and n_C are calculated from equations (6) through (8).

Figures 2a and 2b represent the discussed points for a certain stress state with fixed principal stresses. Fig. 2a is plotted for the case of $n_A < n_C$, and Fig. 2b represents the case $n_A > n_C$. Equation (9) presents all the possible values of one direction cosine for fractures being critically stressed under principal stresses σ_1, σ_2, and σ_3. Note that direction cosines appearing in these equations are calculated for a coordinate system associated with principal axes of stress tensor.

In order to solve the stated problem one needs to determine the interval of possible values of direction cosine *l* standing for critically stressed fractures for every value of *n* inside the interval (9). It is possible to determine the coordinates of points of intersection between circle (5) and raw friction law line for any value of direction cosine *n* from the obtained interval. These points are represented as *D* and *E* (*E* is to the right of *D* on Mohr's diagram, or $\sigma_n^E > \sigma_n^D$, Figures 2c and 2d), and their coordinates are:

For point *D*:

$$\sigma_n^D = \frac{-b - \sqrt{b^2 - 4c}}{2}, \tag{10a}$$

$$\tau_n^D = \mu \cdot \sigma_n^D, \tag{10b}$$

$$b = -\frac{\sigma_1 + \sigma_2}{\mu^2 + 1}, \tag{10c}$$

$$c = -\frac{n^2(\sigma_3 - \sigma_1)(\sigma_3 - \sigma_2) - \sigma_1\sigma_2}{\mu^2 + 1}. \tag{10d}$$

For point *E*:

$$\sigma_n^E = \frac{-b + \sqrt{b^2 - 4c}}{2}, \tag{11a}$$

$$\tau_n^E = \mu \cdot \sigma_n^E, \tag{11b}$$

$$b = -\frac{\sigma_1 + \sigma_2}{\mu^2 + 1}, \tag{11c}$$

$$c = -\frac{n^2(\sigma_3 - \sigma_1)(\sigma_3 - \sigma_2) - \sigma_1\sigma_2}{\mu^2 + 1}, \tag{11d}$$

If these values are introduced into equation (4), the following corresponding values of direction cosine l are obtained:

$$l_D = \sqrt{\frac{\tau_n^{D2} + \left(\sigma_n^D - \frac{\sigma_2 + \sigma_3}{2}\right)^2 - \left(\frac{\sigma_2 - \sigma_3}{2}\right)^2}{(\sigma_1 - \sigma_2)(\sigma_1 - \sigma_3)}}, \tag{12a}$$

$$l_E = \sqrt{\frac{\tau_n^{E2} + \left(\sigma_n^E - \frac{\sigma_2 + \sigma_3}{2}\right)^2 - \left(\frac{\sigma_2 - \sigma_3}{2}\right)^2}{(\sigma_1 - \sigma_2)(\sigma_1 - \sigma_3)}}. \tag{12b}$$

In the same way as before, point E (which is to the right of point D) may geometrically stay outside the area bordered by Mohr's circle. As a result, the corresponding stresses cannot be realized. In order to take into account this opportunity, one has to consider point F – the point of intersection between circle (5) and the outer Mohr's circle – and calculate its coordinates and corresponding value of direction cosine l:

$$l_F = \sqrt{\frac{\tau_n^{F2} + \left(\sigma_n^F - \frac{\sigma_2 + \sigma_3}{2}\right)^2 - \left(\frac{\sigma_2 - \sigma_3}{2}\right)^2}{(\sigma_1 - \sigma_2)(\sigma_1 - \sigma_3)}}, \tag{13a}$$

$$\sigma_n{}^F = \sigma_1 + n^2(\sigma_3 - \sigma_1), \tag{13b}$$

$$\tau_n{}^F = \sqrt{\left(\frac{\sigma_1 - \sigma_3}{2}\right)^2 - \left(\sigma_n{}^F - \frac{\sigma_1 + \sigma_3}{2}\right)^2}. \tag{13c}$$

As a result, for any value of n chosen from the interval (9), one may calculate the interval of the second direction cosine l values to satisfy the critically stressed fractures criterion (1). This interval is dependent on n and has the following form:

$$l \in \left[l_D(n); \quad \min\left(l_E(n); l_F(n)\right)\right]. \tag{14}$$

If one needs to obtain the possible values of the third direction cosine m (cosine of angle between normal vector to a fracture plane and direction of intermediate principal stress σ_2) of critically stressed fractures, usual normalization should be used (l and n are taken from intervals (9) and (14)):

$$m = \sqrt{1 - l^2 - n^2}. \tag{15}$$

Fig. 2 schematically represents the Mohr's diagrams, Mohr's circles, raw friction law, and points *A*, *B*, *C*, *D*, *E*, and *F* with the same notation as above.

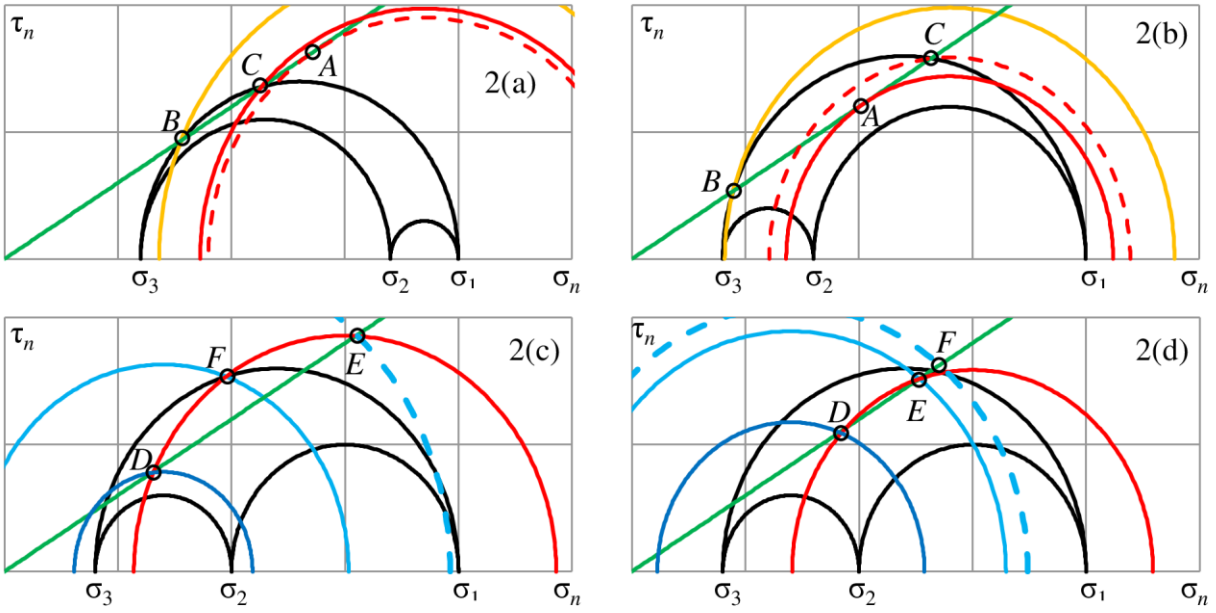

Figure 2. Schematic representation of the Mohr's circles used for theoretical solution.

Figures 2a and 2b are related to equations (6) through (9). Red line represents the circle (5) corresponding to the minimum value of direction cosine *n* from the interval (9); yellow color represents the maximum value of the same interval. Fig. 2a represents the case of $n_A < n_C$, the circle related to n_A value is plotted as dotted line. In the corresponding way, Fig. 2b represents the situation of $n_A > n_C$, with n_C-related circle plotted as dotted line. Figures 2c and 2d are related to equations (10) through (14). At these plots one *n* value is chosen from the interval (9), and red line is related to circle (5). Blue lines represent the circles (4) with the boundary values of *l* from the interval (14). Dark blue line represents the minimum *l* value, and light blue line stands for the maximum value. Two cases are considered in the same way as before $l_E > l_F$ (Fig. 2c) and $l_E < l_F$ (Fig. 2d). Dotted circle is related to the maximum of these two values.

As a result, the algorithm for finding all possible combinations of direction cosines *l* and *n* for given principal stresses σ_1, σ_2, and σ_3 is established. First of all, the coordinates of the critical points *A*, *B*, and *C* and corresponding values of direction cosines n_A, n_B, and n_C are calculated according to equations (6) through (8). The interval of possible values of *n* is determined as (9). Then for each value of *n* inside the calculated interval the coordinates of

critical points *D*, *E*, and *F* and corresponding values of direction cosines l_D, l_E, and l_F are determined according to equations (10) through (13). Finally, for each value of *n* from the interval (9) the interval of corresponding direction cosines *l* is calculated following equation (14). Each pair of direction cosines *l* and *n* is combined with the third cosine *m* obtained from equation (15). As a result, the magnitudes of principal stresses and friction coefficient μ give a certain variety of combinations *l*, *m*, and *n* defining spatial orientations of vectors **n** normal to all critically stressed fractures:

$$\mathbf{n} = \begin{pmatrix} l \in \left[l_D(n); \quad \min\left(l_E(n); l_F(n) \right) \right] \\ m = \sqrt{1 - l^2 - n^2} \\ n \in \left[\max\left(n_A; n_C \right); \quad n_B \right] \end{pmatrix}, \tag{16}$$

Coordinates of the normal vector **n** are given here for a coordinate system related to principal axes of the considered stress tensor.

Despite the study of critically stressed fractures being relatively easy with Mohr's diagram, real data on fractures are typically analyzed using angles, characterizing the fractures' spatial orientations in a certain geographical coordinate system regardless of principal stresses directions and normal vectors to fractures' planes. Such angles include strike and dip angles for example. In order to turn direction cosines into these angles one has to carry out several operations.

Consider a coordinate system with the first axis directed at gravitational force direction, the second axis directed to the East and the third – to the North. An arbitrary stress tensor σ_{ij} is considered in this coordinate system with its components being equal to:

$$\sigma_{ij} = \begin{bmatrix} \sigma_{11} & \sigma_{12} & \sigma_{13} \\ \sigma_{21} & \sigma_{22} & \sigma_{23} \\ \sigma_{31} & \sigma_{32} & \sigma_{33} \end{bmatrix}, \tag{15}$$

The principal values of this positive definite symmetric tensor are determined from characteristic equation (λ are the eigenvalues of (15)):

$$\det(\sigma_{ij} - \lambda\delta_{ij}) = 0, \tag{16}$$

where δ_{ij} is Kronecker delta, $i, j = 1, 2, 3$. This equation has three roots σ_1, σ_2, and σ_3, which are the principal stresses used above. Directions of these principal stresses are determined from system of the equations:

$$\begin{cases} \left(\sigma_{11}-\sigma_k\right)n_1^{\,k}+\sigma_{12}n_2^{\,k}+\sigma_{13}n_3^{\,k}=0, \\ \sigma_{21}n_1^{\,k}+\left(\sigma_{22}-\sigma_k\right)n_2^{\,k}+\sigma_{23}n_3^{\,k}=0, \\ \sigma_{31}n_1^{\,k}+\sigma_{32}n_2^{\,k}+\left(\sigma_{33}-\sigma_k\right)n_3^{\,k}=0, \\ \left(n_1^{\,k}\right)^2+\left(n_2^{\,k}\right)^2+\left(n_3^{\,k}\right)^2=1. \end{cases} \tag{17}$$

Here $k = 1, 2, 3$; $n_p^{\,k}$ is the cosine of an angle between direction of principal stress σ_k and coordinate system axis numbered p ($p = 1, 2, 3$).

As a result, normal vectors **n** to critically stressed fractures planes will have the following coordinates in a global coordinate system:

$$\begin{pmatrix} l_0 \\ m_0 \\ n_0 \end{pmatrix} = \begin{pmatrix} n_1^{\,1} & n_1^{\,2} & n_1^{\,3} \\ n_2^{\,1} & n_2^{\,2} & n_2^{\,3} \\ n_3^{\,1} & n_3^{\,2} & n_3^{\,3} \end{pmatrix} \cdot \begin{pmatrix} l \in \left[l_D(n); \quad \min\left(l_E(n); l_F(n)\right) \right] \\ m = \sqrt{1-l^2-n^2} \\ n \in \left[\max\left(n_A; n_C\right); \quad n_B \right] \end{pmatrix}, \tag{18}$$

where $n_p^{\,k}$ are obtained from equations (17). l_0, m_0, and n_0 are the resultant direction cosines of critically stressed fractures in the introduced global coordinate system. Once the values of n_A, n_B, n_C, $l_D(n)$, $l_E(n)$, and $l_F(n)$ are calculated from principal stresses via equations (6) through (8) and (10) through (13), the posed problem is solved: spatial orientations of critically stressed fractures are obtained for an arbitrary stress tensor σ_{ij} (15). Although it generally solves the posed problem, some further considerations are to be carried out to simplify the further usage of the obtained solution.

Lambert azimuthal equal-area projection (a detailed description of using this projection to analyze strike and dip angles is given by Snyder (1987) and Allmendinger et al. (2012)) will be used in the current study to interpret the direction cosines in terms of structural geology. The following approach is used to show principal stresses' directions on lower hemisphere Lambert equal area stereonet. A sphere of unit radius is constructed from the center of coordinate system; latitude and longitude of the point of intersection between this sphere and vector in direction of

the considered principal stress are calculated. For the coordinate system used in this study latitude φ_k and longitude λ_k of direction of principal stress σ_k are calculated as:

$$\varphi_k = \arctan\left(\frac{n_3^{\,k}}{\sqrt{\left(n_1^{\,k}\right)^2 + \left(n_2^{\,k}\right)^2}}\right), \tag{19a}$$

$$\lambda_k = \arctan\left(\frac{n_2^{\,k}}{n_1^{\,k}}\right). \tag{19b}$$

Each three cosines l_0, m_0, and n_0 of critically stressed fractures are interpreted as longitude and latitude in a way analogous to principal stresses' directions (19) as:

$$\varphi = \arctan\left(\frac{n_0}{\sqrt{\left(l_0\right)^2 + \left(m_0\right)^2}}\right), \tag{20a}$$

$$\lambda_k = \arctan\left(\frac{m_0}{l_0}\right). \tag{20b}$$

As far as equation (18) presents a variety of direction cosines of normal vectors to critically stressed fractures planes, equations (20) give a domain of critically stressed fractures on a stereonet contrary to equations (19) which give nothing more than three dots on the stereonet corresponding to each of the principal stresses.

The overall procedure of obtaining spatial orientations of critically stressed fractures for a given stress tensor σ_{ij} may be formulated as follows: **I.** Calculation of principal stress magnitudes and directions by finding eigenvectors of tensor σ_{ij}. **II.** Calculation of limits on spatial orientation of critically stressed fractures in principal stresses space using equations (6) through (16). **III.** Calculation of direction cosines of the poles to critically stressed fractures planes in a global coordinate system using equation (18). **IV.** Visual representation of the obtained results at stereonet with the help of equations (19) and (20). It seems important to notice that the mentioned procedure may be completed for any arbitrary stress tensor σ_{ij} without any assumptions regarding its direct form (except its symmetry which is typical for the majority of geomechanical problems).

An example of plotted directions of principal stresses corresponding to stress tensor with components σ_{11} = 25 MPa, σ_{22} = 18 MPa, σ_{33} = 8 MPa, $\sigma_{12} = \sigma_{21}$ = –7 MPa, $\sigma_{13} = \sigma_{31}$ = 1 MPa,

$\sigma_{23} = \sigma_{32} = -3$ MPa on lower hemisphere Lambert equal area stereonet is shown in Fig. 3a alongside with the corresponding domains of critically stressed fractures. The following nomenclature will be used hereafter to plot the stereonets: maximum compressive stress σ_1 will be represented by a red dot; intermediate principal compressive stress σ_2 – by a yellow dot; least principal compressive stress σ_3 – by a green dot. Tensile stresses will not be considered. Solid lines (blue in this current case) will serve as boundaries for the domains of critically stressed fractures. Domain of critically stressed fractures is filled with blue in this figure showing the typical area bordered by solid lines – it will not be filled in the subsequent figures. Fig. 3b represents the possible values of direction cosines *l* and *n* calculated from equations (6) through (16) for the considered stress tensor.

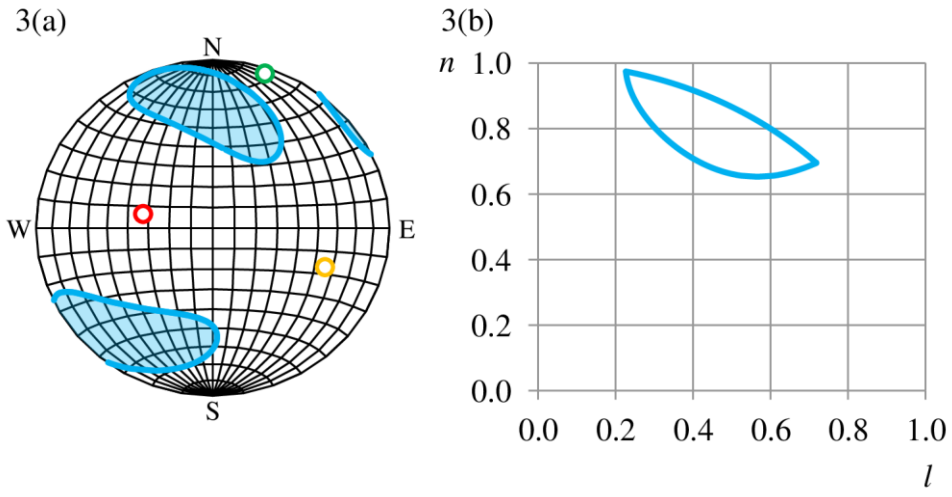

Figure 3. An example of positioning critically stressed fractures at stereonet and direction cosines diagram.

The given example is of illustrative nature. It shows that it is enough to know friction coefficient to determine all possible spatial orientations of fractures being critically stressed in a given stress state characterized by an arbitrary stress tensor σ_{ij}. Despite some difficulties emerging during mathematical description of critically stressed fractures' spatial orientations, the developed algorithm may be applied to the results of geomechanical modeling containing distributions of stress tensor components. It is to be mentioned that all provided equations dealing with stresses are relevant to effective stresses following Biot's theory.

346 The obtained solution presents an opportunity to qualitatively estimate the relative
347 amount of critically stressed fractures. Dubinya and Fokin (2018) proposed the coefficient S_{crit}
348 connected to relative amount of critically stressed fractures as the ratio between the area of
349 domain of critically stressed fractures above the raw friction line at Mohr's diagram (Fig. 1) and
350 the whole area of Mohr's circle. It was discussed that this ratio is equal to the relative amount of
351 critically stressed fractures for a representative volume of an "ideal" rock characterized by
352 uniform distribution of spatial cosines *l* and *n* of natural shear fractures. Although this value
353 can't be directly considered as fraction of critically stressed fractures in rock because uniform
354 distribution of natural fractures orientations is not typical for real rocks, it is possible to consider
355 this value as a qualitative measure of the relative amount of critically stressed fractures. The
356 explicit equations for relative amount of critically stressed fractures S_{crit} are:

357
$$S_{crit} = \frac{8\left(S_{13} - S_{12} - S_{23}\right)}{\pi\left(\left(\sigma_1 - \sigma_3\right)^2 - \left(\sigma_1 - \sigma_2\right)^2 - \left(\sigma_2 - \sigma_3\right)^2\right)}, \tag{21a}$$

358 where S_{ij} (i, j = 1, 2, 3) are non-zero in case of positive value of $(\sigma_i + \sigma_j)^2 - 4(\mu^2 + 1)$ and
359 are equal to:

360
$$S_{ij} = \frac{(\sigma_i - \sigma_j)^2}{8}\left(\begin{array}{l}\arccos B_{ij} - \arccos A_{ij} + \\ + B_{ij}\sqrt{1 - A_{ij}^{\,2}} - A_{ij}\sqrt{1 - B_{ij}^{\,2}}\end{array}\right), \tag{21b}$$

361 where

362
$$A_{ij} = \frac{-\mu^2(\sigma_i + \sigma_j) + \sqrt{(\sigma_i + \sigma_j)^2 - 4(1+\mu^2)\sigma_i\sigma_j}}{(1+\mu^2)(\sigma_i - \sigma_j)}, \tag{21c}$$

363
$$B_{ij} = \frac{-\mu^2(\sigma_i + \sigma_j) - \sqrt{(\sigma_i + \sigma_j)^2 - 4(1+\mu^2)\sigma_i\sigma_j}}{(1+\mu^2)(\sigma_i - \sigma_j)}. \tag{21d}$$

364 As a result, any naturally fractured rock subjected to stresses (15) may be characterized
365 by spatial orientations of fractures that are critically stressed under the given conditions
366 (equations (6) through (18)) and their relative amount obtained from equations (21), which
367 concludes the section devoted to analytical solution of critically stressed fractures spatial
368 orientations problem.

The following sections present some applications of the obtained solution to consider the typical tendencies in critically stressed fractures spatial orientations for variations of stress tensor components.

3 Illustrative examples

The evolution of stereonets representing critically stressed fractures spatial orientations and their relative amount is considered for cases of gradual changes of various parameters of stress tensor (15) or rock properties in this section.

3.1 Principal axes rotation

It is convenient to start analysis of different stress tensors and corresponding critically stressed fractures spatial orientations from the rotation of principal axes of the stress tensor.

It is typical for reservoir geomechanics problems (Zoback, 2007) to consider stress tensor (15) in accordance with well-known Anderson's classification of stress regimes (Anderson, 1951) and new fault types: new formed faults will be normal, strike-slip, or reverse depending on whether the maximum σ_1, intermediate σ_2, or minimum compressive stress σ_3 is directed vertically. These types have been extended to include transitional cases (Philip, 1987; Guiraud et al., 1989) between stress regimes caused by gradual increases in certain components of stress tensor. These transitions may be quantitatively analyzed with introduction of specific tensor shape parameters summarized by Célérier (1995). In the current study the convenient form of generalized stress tensor shape parameter proposed by Simpson (1997) will be used to analyze various stress states from the perspective of critically stressed fractures.

Fig. 4 gives a schematic representation of three Anderson's stress regimes: Normal Fault (σ_1 is directed vertically), Strike-Slip (σ_2 is directed vertically), and Reverse Fault (σ_3 is directed vertically). These three cases are typical for upper layers of the Earth's crust, but, generally speaking, the condition of one of stress tensor principal axes being vertical is only satisfied if the Earth's surface is considered as a free horizontal boundary with no traction. Not every stress state has this property – principal axes may rotate in a vicinity of a major structural weakness.

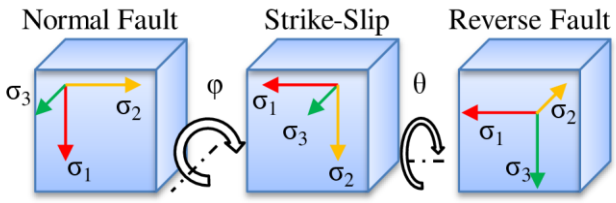

Figure 4. Schematic representation of transition between stress regimes with constant principal stresses magnitudes

Let's consider a hypothetical rotation of stress tensor principal axes using three Euler's angles. It is possible to change all Euler's angles simultaneously providing a complicated evolution of critically stressed fractures spatial orientations. The initial stress tensor σ_{ij}^{0} has its maximum principal stress σ_1 directed vertically and intermediate stress σ_2 directed to the East – a typical Normal Fault stress regime. Initial stress state may be described as:

$$\sigma_{ij}^{0} = \begin{bmatrix} \sigma_1 & 0 & 0 \\ 0 & \sigma_2 & 0 \\ 0 & 0 & \sigma_3 \end{bmatrix}, \quad (22)$$

in the proposed coordinate system (the first axis is vertical, the second is aimed at East; the third is aimed at North).

In the current paper Euler's angles are conventionally introduced to make it possible to transit from initial stress state (22) to the considered stress state (15). Principal stresses are the same for both stress states. Typical z-x-z convention is used here: the first Euler's angle φ stands for rotation of initial stress tensor about initial σ_3 direction (North); the second Euler's angle θ represents rotation about current σ_1 direction (rotations are consecutive); the third Euler's angle ψ stands for rotation about current σ_3 direction (Fig. 4). Note that $\varphi = \theta = \psi = 0$ represents pure Normal Fault regime; the first rotation leads to pure Strike-Slip regime when φ becomes equal to $\pi/2$; the second rotation results in pure Reverse Fault when θ becomes equal to $\pi/2$.

The final directions of principal stresses of stress tensor (15) – solution of equations 17 through may be calculated from the proposed Euler's angles as:

$$\begin{pmatrix} n_1^1 & n_2^1 & n_3^1 \\ n_1^2 & n_2^2 & n_3^2 \\ n_1^3 & n_2^3 & n_3^3 \end{pmatrix} = \begin{pmatrix} \cos\varphi\cos\psi - \cos\theta\sin\varphi\sin\psi & -\cos\psi\sin\varphi - \cos\varphi\cos\theta\sin\psi & \sin\theta\sin\psi \\ \cos\theta\cos\psi\sin\varphi + \cos\varphi\sin\psi & \cos\varphi\cos\theta\cos\psi - \sin\varphi\sin\psi & -\cos\psi\sin\theta \\ \sin\varphi\sin\theta & \cos\varphi\sin\theta & \cos\theta \end{pmatrix}. \quad (23)$$

If principal stresses magnitudes σ_1, σ_2, and σ_3 are fixed, variations φ, θ, $\psi \in (0; \pi)$ cover all the possible stress states with these principal stresses. For example, stress state represented in Fig. 3 may be analyzed from the perspective of Euler's angles as: $\varphi = 10^o$, $\theta = 15^o$, $\psi = 25^o$; principal stresses ratio is: $\sigma_1/\sigma_2/\sigma_3 \approx 4/2/1$.

Figures 5 through 7 represent the described rotations of stress tensor and corresponding changes in critically stressed fractures domain at the stereonet. A particular stress state with ratio $\sigma_1/\sigma_2/\sigma_3$ being maintained as 4/2/1 was analyzed. Friction coefficient is set to 0.6.

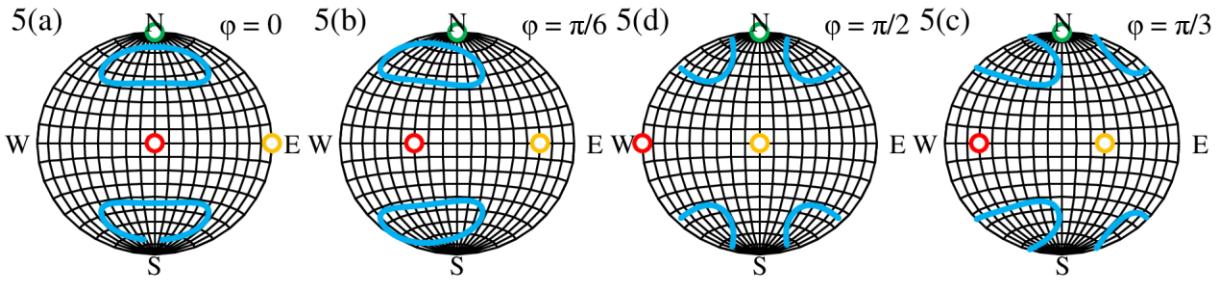

Figure 5. The first rotation about minimum principal stress direction ($\theta = \psi = 0$; φ is gradually increasing).

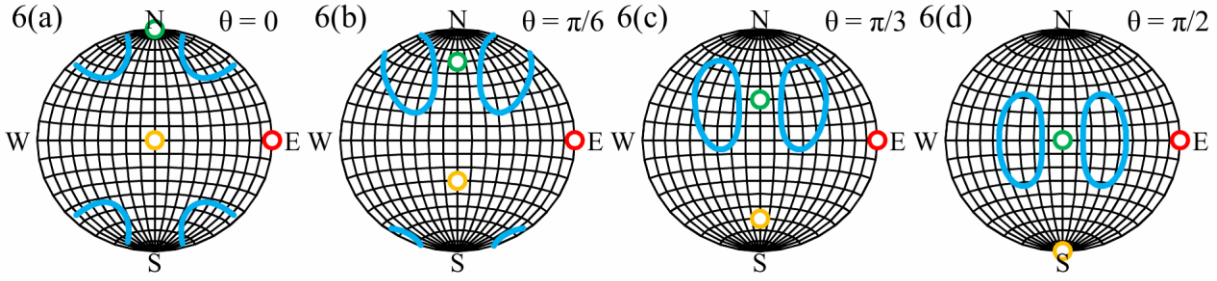

Figure 6. The second rotation about current maximum principal stress direction ($\varphi = \pi/2$, $\psi = 0$; θ is gradually increasing).

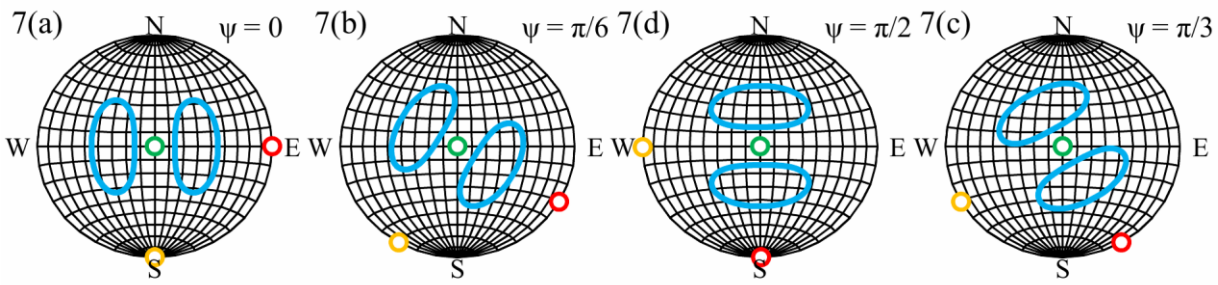

Figure 7. The third rotation about current minimum principal stress direction ($\varphi = \theta = \pi/2$; ψ is gradually increasing)

3.2 Transistional stress regimes

Previous section was devoted to rotation of principal axes of stress tensor with fixed values of principal stresses magnitudes. The next step is analysis of critically stressed fractures behavior under varied principal stresses magnitudes and fixed principal axes.

It is possible to study the relationship between principal stresses through stress tensor shape parameters proposed by Angelier (1979) and developed by Simpson (1997). Shape of any stress tensor may be quantitatively analyzed with the help of shape parameter ϕ that is closely related to Lode-Nadai coefficient:

$$\phi = (\sigma_2 - \sigma_3)/(\sigma_1 - \sigma_3). \quad (24)$$

This definition compares the magnitude of the intermediate stress σ_2 to the other principal stresses: if the intermediate stress is equal to minimum stress, ϕ approaches 0; if it is close to maximum stress, ϕ approaches 1.

There is no information regarding directions of principal axes in this definition, so this parameter was changed to improve its application in geomechanics: if one of the principal axes is aimed vertically, this parameter may be modified to include information about which particular stress is directed vertically. The following modified stress tensor shape parameter A_ϕ was introduced by Simpson (1997):

$$A_\phi = (s + 0.5) + (-1)^s (\phi - 0.5) = (s + 0.5) + (-1)^s \left(\frac{\sigma_2 - \sigma_3}{\sigma_1 - \sigma_3} - 0.5 \right), \quad (25)$$

where s is an index number connected to the considered stress regime: $s = 0$ for normal stress regime (σ_1 is directed vertically, Fig. 5a); $s = 1$ for strike-slip (σ_2 is directed vertically,

Figures 5d and 6a); $s = 2$ for reverse fault (σ_3 is directed vertically, Fig. 7). A_ϕ ranges continuously from 0 to 1 for normal, from 1 to 2 for strike-slip, and from 2 to 3 for reverse fault stress regimes.

The proposed analytical solution to spatial orientations of critically stressed fractures makes it possible to obtain these orientations for transitions between stress regimes caused by gradual changes in stress tensor shape parameters.

Consider an initial stress tensor σ_{ij}^0 with principal stresses ratio $\sigma_1/\sigma_2/\sigma_3 = 4/1/1$; $\phi = 0$, $A_\phi = 0$, Normal Fault stress regime. Only principal stresses will be changed in this section, so Euler's angles discussed in the previous section will be fixed. Critically stressed fractures has been studied in an analogous way by Davidson et al. (2012) for a particular geothermal field with maximum horizontal stress azimuth 56^o, so the Euler's angles were chosen as $\varphi = 0^o$, $\theta = 56^o$, $\psi = 0^o$ to provide an opportunity to verify the obtained critically stressed fractures patterns. Once again, all the procedures may be carried out for any combination of Euler's angles.

There are different opportunities to adjust stress tensor shape. Fig. 8 presents transition between stress regimes caused by gradual increase of A_ϕ from 0 to 3 with fixed stresses σ_1 and σ_3, under varied $\sigma_1 = \sigma_3 + A_\phi \cdot (\sigma_1 - \sigma_3)$. Isolines of different color are borderlines of domains of critically stressed fractures for corresponding values of stress tensor shape coefficients. Fig. 8a shows domains of critically stressed fractures for increasing A_ϕ for Normal Fault; Fig. 8b shows domains of critically stressed fractures for increasing A_ϕ for Strike-Slip; Fig. 8c shows domains of critically stressed fractures for increasing A_ϕ for Reverse Fault. Fig. 8b is analogous to the one obtained by Davidson et al. (2012) (see Davidson et al. (2012), Fig. 8) and is in full quantitative agreement with their results.

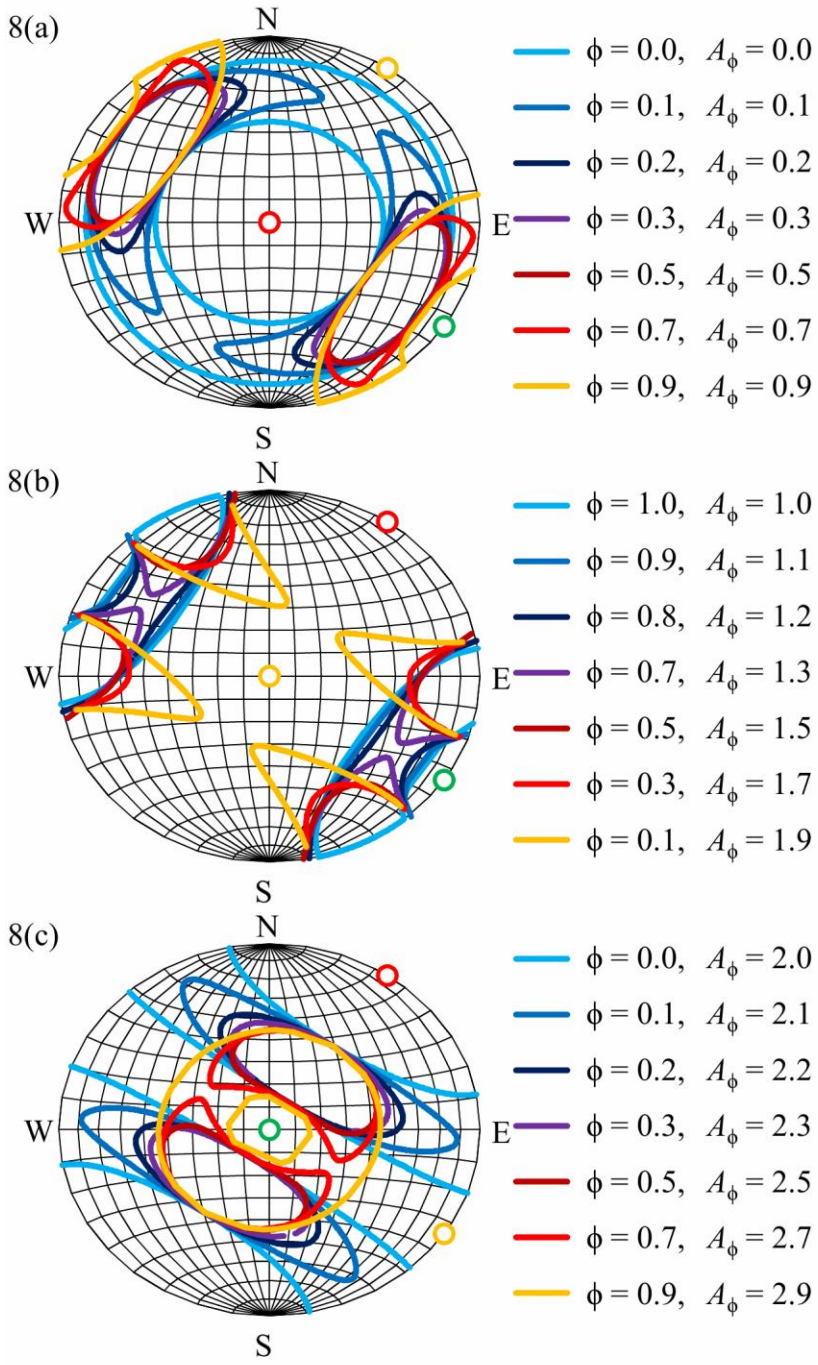

Figure 8. Transitions between stress regimes under fixed principal stresses directions and varied stress tensor shapes.

It can be clearly seen that the domains of critically stressed fractures are axis-symmetric for the cases of A_ϕ = 0, 1, 2 which comes naturally from equations (1) through (3).

Critically stressed fractures domains show similar behavior under different ratios σ_1/σ_3. As a result, variations of A_ϕ and σ_1/σ_3 ratios cover all possible principal stresses magnitudes. These variations are summarized in Fig. 9 where relative amount of critically stressed fractures S_{crit} introduced in equation (21) is plotted for different stress tensor shape parameters.

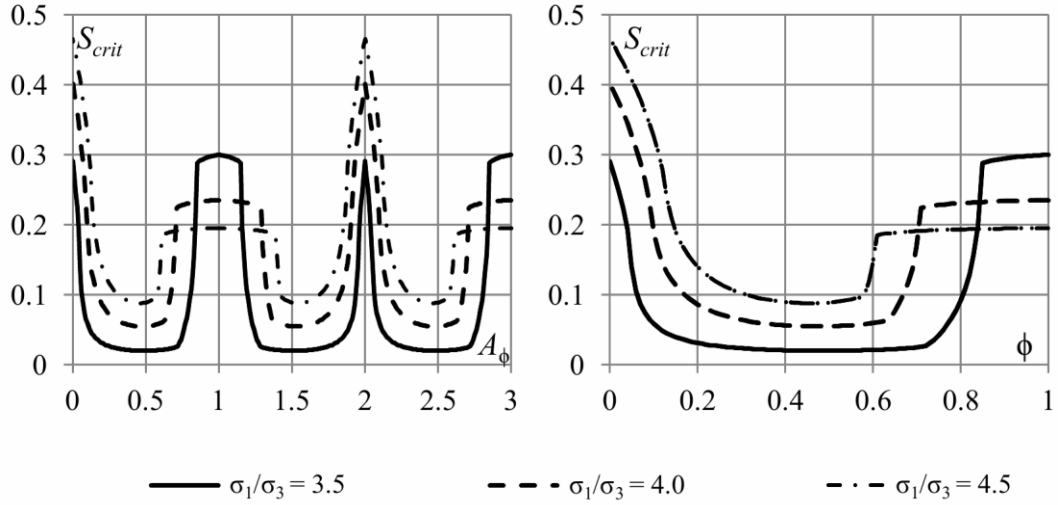

Figure 9. Relative amount of critically stressed fractures during transitions between stress regimes under fixed principal stresses directions and varied stress tensor shapes.

Note that no critically fractures emerge if:

$$\frac{\sigma_1}{\sigma_3} \geq \frac{\sqrt{\mu^2+1}+\mu}{\sqrt{\mu^2+1}-\mu}, \tag{26}$$

following from equations (1) through (3). For the considered case of $\mu = 0.6$, minimum ratio between maximum and minimum principal stress, providing an opportunity for critically stressed fractures to emerge, is about 3.12. The maximum possible ratio between maximum and minimum principal stresses is governed by rock strength properties. Fig. 9 represents evolution of critically stressed fractures relative amount for a set of principal stresses ratios: $\sigma_1/\sigma_3 = 3.5$, 4.0, 4.5. As it can be clearly seen from equations (21), type of stress regime is not important for relative amount of critically stressed fractures: only relationships between principal stresses magnitudes matter. As a result, the same stress tensor shape parameter ϕ corresponding to different generalized stress tensor shape parameters A_ϕ for different stress regimes provide the same relative amont of critically stressed fractures. The following tendency is observed: relative

amount of critically stressed fractures is the greatest for $\phi = 0$ and 1, and the least in the middle of transition with $\phi \approx 0.5$. The largest changes in relative amount of critically stressed fractures appear when ϕ changes from 0 to 0.1 and when it exceeds 0.6.

3.3 Denendency on friction coefficient

Friction coefficient μ is the last parameter to analyze in the current study. All the previous calculations were completed for a fixed friction coefficient $\mu = 0.6$. It is clear that an increase in friction coefficient will lead to a corresponding decrease of domain of critically stressed fractures.

Fig. 10 represents the evolution of critically stressed fractures domains at stereonets for a set of typical fixed stress tensor shape parameters: A_ϕ = 0.3; 0.7; 1.3; 1.7; 2.3; 2.7 covering all transitional stress regimes. Color represents different values of friction coefficient μ = 0.4; 0.5; 0.6; 0.7 with darker colors representing higher friction coefficients. It can be easily seen that an increase in friction coefficient really leads to contraction of critically stressed fractures domain with its center being close to spatial orientations of optimally oriented faults (Zoback, 2007). This evolution is analyzed in the same way as in the previous section: Fig. 11 represents changes in relative amount of critically stressed fractures obtained from equations 21 as a function of friction coefficient for a fixed stress tensor shape parameter ϕ. Once again, same values of stress tensor shape parameter ϕ obtained for different generalized stress tensor shape parameters A_ϕ ($A_\phi = \phi$ for Normal Fault; $A_\phi = 2 - \phi$ for Strike-Slip; $A_\phi = 2 + \phi$ for Reverse Fault) provide the same relative amount of critically stressed fractures S_{crit} because stress regime is not considered in equations (21).

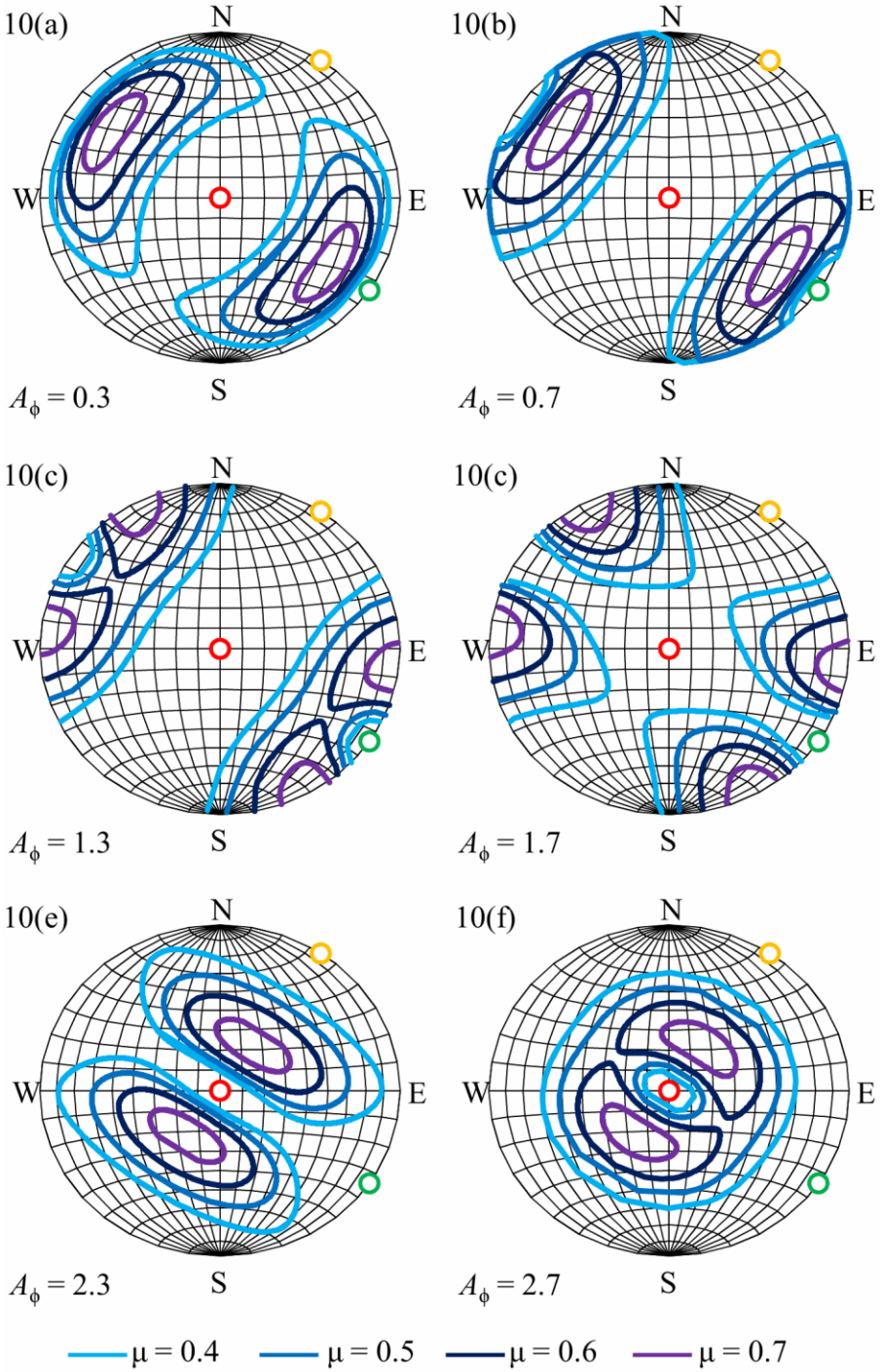

520

521 **Figure 10.** Critically stressed fractures domains for varied friction coefficient.

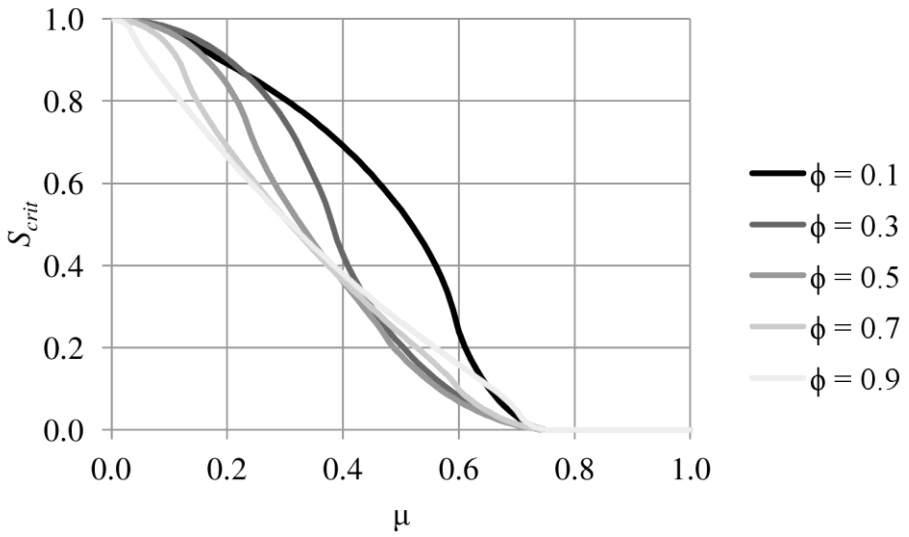

522

523 **Figure 11.** Relative amount of critically stressed fractures for varied friction coefficient

524 It is obvious from Fig. 11 that an increase in friction angle leads to a nonlinear decrease
525 in relative amount of critically stressed fractures. Although Fig. 11 is plotted for a fixed principal
526 stresses ratio $\sigma_1/\sigma_3 = 4/1$ and varied intermediate principal stress σ_2 (same as Fig. 8), this
527 evolution is similar for other σ_1/σ_3 ratios: the plot moves to the right for the greater ratios. S_{crit}
528 becomes zero once raw friction law becomes higher than Mohr circle. The possible values of
529 friction coefficient μ corresponding to presence of critically stressed fractures may be directly
530 calculated from equation (26):

531
$$\mu \le \frac{\sigma_1/\sigma_3 - 1}{2\sqrt{\sigma_1/\sigma_3}}. \qquad (27)$$

532 Magnitudes and directions of principal stresses alongside with friction coefficient of the
533 rock are the only parameters influencing spatial orientations and relative amount S_{crit} of critically
534 stressed fractures. In these sections each one of these parameters was analyzed from the
535 perspective of critically stressed fractures spatial orientations and relative amount: Figures 5, 6,
536 and 7 are focused on critically stressed fractures domains evolution caused by changes in
537 principal stresses directions; Figures 8 and 9 are related to gradual changes of principal stresses
538 magnitudes; and finally, Figures 10 and 11 deal with friction coefficient. As a result, any
539 arbitrary stress tensor may be considered as combination of these three cases proving that the

proposed analytical solution is indeed suitable to understand critically stressed fractures patterns for any geomechanical problem.

4 Conclusions

The obtained analytical solution makes it possible to calculate all possible spatial orientations of critically stressed fractures for an arbitrary stress tensor acting in a fractured rock mass with a known friction coefficient.

Taking into account numerous papers devoted to establishing the relationship between critically stressed and hydraulically conductive fractures, knowledge of spatial orientations of critically stressed fractures is an important step to understand the filtration paths in naturally fractured rocks.

The proposed mathematical algorithm is strongly dependent on the input data – the spatial distributions of stress tensor components. As far as these data are among the main results of geomechanical modeling, which is frequently carried out at the current state of scientific and engineering approaches to reservoir development, the proposed algorithm can be easily integrated into existing solutions for geomechanical modeling. At the same time, such an integration will increase the value of geomechanical modeling results without considerable changes in costs as far as all the equations (6) through (16) are analytical.

According to the problem being solved during geomechanical modeling, one may use the obtained analytical solution to consider specific processes in terms of critically stressed fractures. The following problems of reservoir geomechanics may be particularly analyzed: forecast of critically stressed fractures near a hydraulic fracture and creation of a branching network of hydraulically conductive fractures through fluid injection; analysis of evolution of critically stressed fractures' properties throughout reservoir development based on results of four-dimensional geomechanical modeling and others; wellbore stability in fractured reservoirs and other problems of reservoir geomechanics. It is also likely that there are other areas to apply the obtained solution.

Spatial orientations of critically stressed fractures are the main focus of the current paper, but there are also many important properties of the fractured medium not considered here. These properties include sizes of the fractures, conductivity properties, shape and connectivity of the

fractures and others. Scaling factor was not considered in the current paper as well. The last results of modeling the behavior of naturally fractured rock masses prove that these factors may be taken into account if petroelastic modeling approaches are applied to predict effective mechanical properties of fractured rock masses. It is worth to be highlighted that the analysis of spatial orientations of critically stressed fractures should be completed beforehand leading to increase in quality and reliability of input data for petroelastic modeling.

Acknowledgments, Samples, and Data

The authors declare that they have no conflict of interest.

The reported study was funded by RFBR, project number № 20-05-00629.

As far as the paper is theoretical, data were not used, nor created for this research.

The author would like to thank his colleagues Sergey Tikhotskiy, Irina Bayuk, and Kirill Ezhov for their encouragement and help on the earier stages of the his study of critically stressed fractures. The author would also like to thank Marina Dubinya for insightful comments on an earlier draft of this manuscript.

References

Allmendinger, R. W., Cardozo, N., & Fisher D. M. (2012). *Structural Geology Algorithms Vectors and Tensors*. Cambridge: Cambridge University Press.

Anderson, E. M. (1951). The Dynamics of Faulting and Dyke Formation With Application to Britain. Edinburgh: Oliver and Boyd.

Angelier, J. (1979). Determination of the mean principal stresses for a given fault population. *Tectonophysics*, *56*(3–4), T17–T26. https://doi.org/10.1016/0040-1951(79)90081-7

Barton, C. A., Zoback, M. D., & Moos, D. (1995). Fluid flow along potentially active faults in crystalline rocks. *Geology*, *23*(8), 683–686. https://doi.org/10.1130/0091-7613(1995)023<0683:FFAPAF>2.3.CO;2

Bayuk, I. O., Dubinya, N. V., Garagash, I. A., Tikhotskiy, S. A., & Tikhotskaya, O. A. (2019). *Multiscale Rock-Physics Modeling of Effective Elastic Properties of Fractured Reservoir Rocks.*

595 Paper presented at 53rd US Rock Mechanics/Geomechanics Symposium, American Rock
596 Mechanics Association, New York City, NY.

597 Biot, M. A. (1955). Theory of elasticity and consolidation for a porous anisotropic solid. *Journal*
598 *of Applied Physics*, *26*(2), 182–185. https://doi.org/10.1063/1.1721956

599 Bisdom, K., Bertotti, G., & Nick, H. M. (2016). The impact of different aperture distribution
600 models and critical stress criteria on equivalent permeability in fractured rocks. *Journal of*
601 *Geophysical Research: Solid Earth*, *121*(5), 4045–4063. https://doi.org/10.1002/2015JB012657

602 Byerlee, J. (1978). Friction of Rocks. *Pure and Applied Geophysics*, *116*, 615–626.
603 https://doi.org/10.1007/BF00876528

604 Célérier, B. (1995). Tectonic regime and slip orientation of reactivated faults. *Geophysical*
605 *Journal International*, *121*(1), 143–161. https://doi.org/10.1111/j.1365-246X.1995.tb03517.x

606 Chan, A. W., Brem, A. G., & Abd Rahim, M. H. (2019). *Lost Circulations Due to Fault*
607 *Reactivation and the Implications on Stress Characterization*. Paper presented at 53rd US Rock
608 Mechanics/Geomechanics Symposium, American Rock Mechanics Association, New York City,
609 NY.

610 Coussy, O. (2004). *Poromechanics*. West Sussex: John Wiley & Sons Ltd.

611 Davatzes, N. C. & Hickman, S. H. (2010). *The Feedback Between Stress, Faulting, and Fluid*
612 *Flow: Lessons from the Coso Geothermal Field, CA, USA*. Paper presented at World Geothermal
613 Congress, International Geothermal Association, Bali, Indonesia.

614 Davidson, J., Siratovich, P., Wallis, I., Gravley, D., & McNamara, D. (2012). Quantifying the
615 stress distribution at the Rotokawa geothermal field, New Zealand. Paper presented at New
616 Zealand Geothermal Workshop, Auckland, New Zealand.

617 Dubinya, N. (2019). *Stress state estimation based on local variations of effective elastic moduli*
618 *caused by presence of critically stressed fractures*. Paper presented at 53rd US Rock
619 Mechanics/Geomechanics Symposium, American Rock Mechanics Association, New York City,
620 NY.

621 Dubinya, N. V., & Ezhov, K. (2017). A. In-situ horizontal stress estimation based on the
622 geometrical properties of fractures in well vicinity. *Geophysical Research*, 18(2), 5–26.
623 https://doi.org/10.21455/gr2017.2-1

624 Dubinya, N. V., & Fokin, I. V. (2018). *Nonlinear Model for Reversible Deformation of Rock*
625 *Containing Critically Stressed Fractures*. Paper presented at 52nd U.S. Rock
626 Mechanics/Geomechanics Symposium, American Association of Rock Mechanics, Seattle, WA.

627 Fisher, Q. J., Casey, M., Harris, S. D., & Knipe, R. J. (2003). Fluid-flow properties of faults in
628 sandstone: The importance of temperature history. *Geology*, *31*(11), 965–968.
629 https://doi.org/10.1130/G19823.1

630 Guiraud, M., Laborde, O., & Philip, H. (1989). Characterization of various types of deformation
631 and their corresponding deviatoric stress tensors using microfault analysis. *Tectonophysics*,
632 *170*(3-4), 289–316. https://doi.org/10.1016/0040-1951(89)90277-1

633 Hickman, S. H., Barton, C. A., Zoback, M. D., Morin. R., Sass, J., & Benoit, R. (1997). In situ
634 stress and fracture permeability along the Stillwater fault zone, Dixie Valley, Nevada.
635 *International Journal of Rock Mechanics and Mining Sciences & Geomechanics Abstracts*, *34*
636 (3–4), 414. https://doi.org/10.1016/S0148-9062(97)00169-1

637 Ito, T., Fujii, R., Evans, K. F., & Hayashi, K. (2002). Estimation of Stress Profile with Depth
638 from Analysis of Temperature and Fracture Orientation Logs in a 3.6 km Deep Well at Soultz,
639 France. Paper presented at SPE/ISRM Rock Mechanics Conference, Society of Petrolum
640 Engineers, Irwing, TX. https://doi.org/10.2118/78185-MS

641 Ito, T., & Zoback, M. D. (2000). Fracture permeability and in situ stress to 7 km depth in the
642 KTB scientific drillhole. *Geophysical Research Letters*, *27*(7), 1045–1048.
643 https://doi.org/10.1029/1999GL011068

644 Kolditz, O., Gorke, U. J., Shao. H., & Wang, W. (2016). *Thermo-Hydro-Mechanical-Chemical*
645 *Processes in Porous Media: Benchmarks and Examples.* Switzerland: Springer International
646 Publishing.

647 Ligtenberg, J. H. (2005). Detection of fluid migration pathways in seismic data: implications for
648 fault seal analysis. *Basin Research*, *17*, 141–153. https://doi.org/10.1111/j.1365-
649 2117.2005.00258.x

650 Massiot, C., Nicol, A., McNamara, D. D., & Townend, J. (2017). Evidence for tectonic,
651 lithologic, and thermal controls on fracture system geometries in andesitic high-temperature
652 geothermal field. *Journal of Geophysical Research: Solid Earth*, *122*(8), 6853–6874.
653 https://doi.org/10.1002/2017JB014121

654 Mattila, J. & Follin, S. (2019) Does In Situ State of Stress Affect Fracture Flow in Crystalline
655 Settings? *Journal of Geophysical Research: Solid Earth*, *124*(5), 5241–5253.
656 https://doi.org/10.1029/2018JB016791

657 Philip, H. (1987). Plio-Quaternary evolution of the stress field in Mediterranean zones of
658 subduction and collision. *Annales geophysicae. Series B. Terrestrial and planetary physics*, *5*(2),
659 301–319.

660 Rogers, S. (2003). Critical stress-related permeability in fractured rocks. Fracture and in situ
661 stress characterization of hydrocarbon reservoirs. *Geological Society, London, Special*
662 *Publications*, *209*(1), 7–16. https://doi.org/10.1144/GSL.SP.2003.209.01.02

663 Sathar, S., Reeves, H. J., Cuss, R. J., & Harrington, J. F. (2012). The role of stress history on the
664 flow of fluids through fractures. *Mineralogical Magazine*, *76*(8), 3165–3177.
665 https://doi.org/10.1180/minmag.2012.076.8.30

666 Schwab, D. R., Bidgoli, T. S., & Taylor, M. H. (2017). Characterizing the potential for injection-
667 induced fault reactivation through subsurface structural mapping and stress field analysis,
668 Wellington Field, Sumner County, Kansas. *Journal of Geophysical Research: Solid Earth*, *122*,
669 10,132–10,154. https://doi.org/10.1002/2017JB014071

670 Silva, I., Domingos, F., Marinho, P., Laronga, R., & Khan, S. (2003). *Advanced Borehole Image*
671 *Applications in Turbidite Reservoirs Drilled With Oil Based Mud: A Case Study From Deep*
672 *Offshore Angola*. Paper presented at SPWLA 44th Annual Logging Symposium, Society of
673 Petrophysicists and Well-Log Analysts, Galveston, TX.

674 Simpson, R. W. (1997). Quantifying Anderson's fault types. *Journal of Geophysical Research:*
675 *Solid Earth*, *102*(B8), 17,909–17,919. https://doi.org/10.1029/97JB01274

676 Snyder, J. P. (1987). *Map Projections – A Working Manual*. Washngton D.C.: U.S. Government
677 Printing Office.

678 Townend, J., Zoback, M. D. (2000). How faulting keeps the crust strong. *Geology*, *28*(5), 399–
679 402. https://doi.org/10.1130/0091-7613(2000)28<399:HFKTCS>2.0.CO;2

680 Zhu, H., Jin, X., Guo, J., An, F., Wang, Y., & Lai, X. (2016). Coupled flow, stress and damage
681 modelling of interactions between hydraulic fractures and natural fractures in shale gas
682 reservoirs. *International Journal of Oil, Gas and Coal Technology*, *13*(4), 359–390.
683 http://dx.doi.org/10.1504/IJOGCT.2016.080095

684 Zoback, M. D. (2007). *Reservoir Geomechanics*. Cambridge: Cambridge University Press.